Available online at www.sciencedirect.com

ScienceDirect

Proceedings of the Combustion Institute 39 (2023) 3293–3302

Proceedings of the Combustion Institute

www.elsevier.com/locate/proci

Pore-Resolving Simulations of Biomass Char Particle Combustion

Dongyu Liang, Simcha Singer*

Department of Mechanical Engineering, Marquette University, Milwaukee, WI 53233

Received 5 January 2022; accepted 12 July 2022
Available online 8 September 2022

Abstract

Biomass char morphology affects combustion behavior at the particle scale for zone II conditions, in which both heterogeneous reaction and intra-particle diffusion govern the overall rate. Furthermore, particle-scale processes affect reactor-scale outputs, and reactor-scale simulations are sensitive to particle-scale models. However, most char particle combustion models employ coarse-grained, effective-continuum approaches, which treat all porosity at the subgrid-scale. Effective-continuum approaches are not valid or accurate in the presence of large, irregular pores which can approach the size of the particle. A 3-D, pore-resolving CFD simulation approach using real biomass char particle geometries obtained from X-ray micro-computed tomography (micro-CT) is therefore used to examine the impact of morphology on zone II combustion for pulverized (~100 μm) biomass char particles for the first time. In contrast to larger, millimeter to centimeter sized particles, the sub-millimeter, high aspect ratio biomass char particles exhibited localized reactant penetration into the innermost regions of the particles, facilitated by the presence of large pores connected to the external surface. The oxygen mole fraction distributions were governed by the large pore morphology, were non-monotonic with distance from the surface, and achieved minima in thick microporous char regions surrounding the large pores. A comparison between the pore-resolving simulation and an equivalent, spatially resolved, effective-continuum simulation revealed that even in the microporous char, the effective-continuum model underpredicted reactant penetration. A careful comparison was then performed between 30 pore-resolving particle simulations and several effectiveness factor models that employed particle-specific parameters. Commonly used uniform cylinder models significantly underpredicted effectiveness factors for these real pulverized pine char particles, while accessible hollow cylinder models achieved less than 10% relative error when averaged over all 30 particles.

Keywords: Pore-scale simulation; Biomass; Char combustion; Micro-CT; Effectiveness Factor

1. Introduction

Due to environmental concerns, biomass gasification, oxy-combustion, and co-firing with coal have gained interest as strategies for electricity generation [1]. During biomass combustion in pulverized fuel boilers and furnaces, sub-millimeter

---

* Corresponding author.
E-mail address: simcha.singer@marquette.edu (S. Singer).

https://doi.org/10.1016/j.proci.2022.07.098
1540-7489

particles undergo devolatilization, producing light gases, tars, and porous char particles, which are subsequently oxidized. Due to its relatively slow rate compared to volatile production and oxidation, char combustion is typically the rate-limiting process.

Char morphology has a strong impact on the rate of combustion for industrially-relevant "zone II" conditions [2–4], in which heterogeneous reaction and diffusion in the porous particles both govern the char combustion rate. Particle-scale processes affect reactor-scale outputs [5–7], and reactor-scale computational fluid dynamic (CFD) simulations are sensitive to the models used for char particles [6–8], even for biomass [6,8] with its lower fixed carbon than coal. Furthermore, the distribution of biomass particle morphologies must be correctly modeled to obtain accurate reactor-scale predictions [5,9]. Therefore, an understanding of the impact of biomass char morphology on particle-scale combustion is needed to design and accurately model biomass combustion systems.

Biomass char morphology depends on the fuel's cellulose, hemicellulose, and lignin content, cell wall characteristics, and devolatilization conditions, such as the heating rate [10,11]. Irregular void structures, cenospheres, and dense chars have been observed [4,10–12], as well as features not typical of coal char, such as high aspect ratios, large cellular structures, and anisotropic pores [2,11,13]. Chars possess a range of pore sizes, from micropores, mesopores, and macropores, to "large pores" and "voids" with sizes that approach that of the particle [4]. Because the surface area on the small pore walls exceeds the external particle area by orders of magnitude [10,14], heterogeneous reactions occur primarily within the particles, even in the presence of diffusion limitations.

Most single particle char combustion models, whether detailed simulations or simple 1-D models used in reactor-scale CFD, employ the effective continuum assumption, which treats all porosity at the subgrid-scale, irrespective of the pore size. Effective-continuum (or "upscaled") models solve conservation equations for a composite region composed of solid and pores. However, effective-continuum models are only valid and accurate when the size of the pores is much smaller than the size of the particle [15],

$$L_{pores} \ll L_{particles}. \tag{1}$$

This is not the case for many biomass chars, which are morphologically complex and contain pores with sizes on the same scale as the particle itself [4,11]. It has been shown experimentally and numerically that effective continuum models cannot accurately predict "zone II" combustion and gasification [3,16–18].

X-ray micro-computed tomography (micro-CT), which can image the internal and external structure of char particles in three dimensions (3-D), can help elucidate the impact of real morphology during char combustion [2,19]. "Morphology" refers here to geometrical features and large pores (larger than a few microns) which affect gas diffusion throughout the particle. Micro-CT (135 μm voxels) was recently used to image the evolution of solid density and gas temperature in large (∼19 mm), smoldering biomass particles in-situ, and revealed the importance of biomass structure (e.g., cracks) on char oxidation [20]. A subsequent study found that pore orientation affected volatile transport, while char oxidation was largely confined to the edges of 16 mm particles [21]. Micro-CT (2 μm voxels) was also used in conjunction with zone II experiments to qualitatively examine the impact of anisotropy, pore morphology, and gas transport on the evolution of cylindrical wood char particles (2 mm) [2]. For cylindrical biomass char with large pores (>5 μm) oriented along the particle axis, gasification likewise proceeded primarily in the axial direction rather than in the radial direction.

Micro-CT has also been used to generate geometries for 3-D, pore resolving CFD simulations to examine the impacts of real char morphology during gasification [17] and combustion [18]. Bituminous coal char particles (∼100 μm) were imaged with high-resolution micro-CT (1.6 μm voxels) to resolve internal and external structures, including large pores for which upscaling is not appropriate. The large pores were fully resolved in the geometry and standard gas-phase conservation equations were solved in those regions, as well as in a surrounding gas boundary layer. Effective-continuum equations were employed only in the surrounding char ("microporous char"), where the upscaling constraints (Eq. (1)) are satisfied due to the small pore sizes. The reactant (oxygen) mole fraction distribution in *real* char particles was highly dependent on the large pore morphology and connectivity for zone II conditions, as particles with connected large pores that extended to the surface experienced enhanced gas diffusion throughout the particle [18]. To assess engineering models used in reactor-scale CFD codes, several 1-D effectiveness factors models were compared to effectiveness factors calculated from volume integration of 3-D pore-resolving data. Particles with one central void were accurately modeled as 1-D hollow spheres, but the behavior of more complex particles could not be accurately predicted by the simpler 1-D models [18].

In this paper, 3-D pore-resolving simulations based on micro-CT are applied to study combustion of small (∼100 μm diameter) biomass char particles for the first time. The simulations are used to examine the dependence of oxygen penetration and temperature on real biochar morphology for zone II conditions and for particle sizes typical of biomass (oxy-)combustion and co-firing in pulverized fuel boilers. Results from the geometrically faithful simulations are compared to an equivalent, spatially resolved effective-continuum model, and are used to evaluate the performance of several simpler effectiveness factor models which are amenable for use as particle-scale models in reactor-scale CFD codes.

2. Methods and Models

2.1. Biomass Char Preparation

Pine sawdust from a woodworking facility (Larrabee, Iowa) was sieved to 100 μm. Biomass particles were dispersed in a single layer on a sheet of aluminum foil, covered with a beaker, purged with nitrogen, and sealed. To produce char at a high heating rate, the inverted beaker was placed in a pre-heated muffle oven at 1073 K for 30 s. The initial heating rate was estimated to exceed 10^3 K/s, although it was lower than what would be achieved in real pulverized fuel boilers.

2.2. Micro-CT Imaging and Meshing

Dozens of biomass char particles were imaged simultaneously using a high-resolution micro-CT (GE v|tome|x s 240) operating at 60 kV and 190 μA, with a voxel size of 2.00 μm. The resolution was chosen to balance the need to image many particles at once, with the need to resolve pores larger than a few microns which violate the constraints for upscaling and cannot be treated at the subgrid-scale. Following reconstruction, the TIFF stack was imported into ScanIP (Synopsys, Mountain View, USA). Thirty particles were able to be separated and segmented from one another and from the support. For each particle, a recursive Gaussian filter was applied, and grey-scale thresholding was used to segment the resolved “large pores” from the “microporous char” which was comprised of carbonaceous solid and unresolved porosity.

To focus on the impacts of morphology, all particles were isotropically scaled by a small factor such that the total volume of each char particle (which includes the volume of microporous char and resolved pores) was identical. Morphological measurements for each particle were then performed (Table S1). Individual biomass char particles were placed in the center of a spherical domain with a diameter of 1300 μm, which was meshed with tetrahedra using Scan IP’s “+FE Free” algorithm. Approximately two million mesh elements were used for every biomass char particle and its surroundings, based on a mesh convergence study [18]. The meshes were fine in and around the 3-D particles and became progressively coarser with distance from the particles into the surrounding gas boundary layer.

2.3. Pore-Resolving Simulations

The 3-D pore-resolving simulation approach is outlined here, as it has been detailed elsewhere [17] and in the Supplementary Material (with a nomenclature in Table S2). Far-field boundary conditions (1373 K and mole fractions of 12% O_2, 10% H_2O, 74% CO_2, and 4% CO) were applied at the edge of the domain and were based on experimental conditions just outside the volatile flame in a 100 kWth pilot-scale furnace [22]. Particles were assumed to be perfectly entrained in the flow, so no relative (slip) velocity was imposed, although the boundary velocity was free to adjust itself according to Stefan flow effects arising from heterogeneous reaction. Due to the very small length scales, the flow remains laminar.

A cross-section of a typical segmented and meshed particle is shown in Fig. 1. The large pores (blue regions), which violate the size constraints for an effective continuum treatment, were fully resolved in the geometry, and standard gas-phase conservation equations (mass, momentum, species, and energy) were applied in those regions. The same first-principles conservation equations were applied in the gas boundary layer surrounding the particles (green regions). For the “microporous char” (red regions), which contain much smaller micropores, mesopores, and macropores that satisfy the size constraints for upscaling (Eq. (1)), effective-continuum conservation equations were applied (for mass, momentum, species, and energy). It is noted that source terms are present in all effective-continuum conservation equations, even the mass conservation equation, which contains a source term to account for gas species generated due to heterogeneous reaction, which occurs on the surface of unresolved pores in the microporous char. The ideal gas equation of state was employed for these high-temperature, atmospheric pressure combustion simulations.

Char oxidation was modeled using a first-order rate expression (see Table S3) [14]. Submodels for transport in the microporous char accounted for both Knudsen and molecular diffusion [17]. Molecular diffusion coefficients were calculated using the mixture-averaged formulation and viscosity and thermal conductivities were calculated using kinetic theory and standard mixing rules. Homogenous reactions were neglected due to the small particle size, which minimizes their importance [23]. Radiation was neglected because it is assumed to be dominated by particle-particle radiation amongst nearby particles of similar temperature. Gasification reactions were not considered because they are orders of magnitude slower than oxidation at the conditions simulated. To focus on the impact of morphology, the unresolved porosity, and the sub-grid-scale surface area per unit volume of the microporous char regions were the same for every

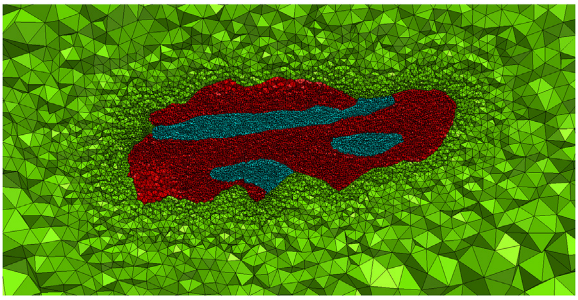

Fig. 1. Cross-section of a portion of a meshed simulation domain for a typical biomass char particle, showing the surrounding gas (green), microporous char (red), and resolved pores (blue).

particle, as were all transport, thermodynamic, and kinetic parameters. Isotropic properties were employed at the subgrid-scale to avoid imposing any assumptions about the morphology beyond what could be resolved.

Species and temperature distributions in and around reacting char particles are approximately quasi-steady at most times [24,25], so a transient solution is closely approximated by a series of steady-state solutions at different levels of char conversion. This has been confirmed in the context of pore-resolving simulations of real coal char particles [18]. Although, in reality, the morphology changes as carbon is consumed, the change is relatively gradual for entrained particles and may become abrupt only late in conversion. Steady-state simulations therefore provide accurate solutions for a *given morphology,* since transient solutions would essentially correspond to a series of slightly differing morphologies. Steady-state simulations were performed in Fluent (Ansys, Canonsburg, USA) using the pressure-based solver and the fully coupled algorithm. To ensure that the CFD simulations were comparable to the simpler models outlined below (Sections 2.4 and 2.5), the simulation has been verified using an ideal geometry and comparing the numerical results with an analytical solution.

In analyzing the interplay of reaction and diffusion in porous particles, the effectiveness factor, η, is a key metric that represents the ratio of the actual, diffusion-limited reaction rate integrated over a particle's volume, to the ideal reaction rate in the absence of any diffusion limitations. In reactor-scale CFD codes, particle models calculate the actual reaction rate by solving a simple, analytical model for η and multiplying by the ideal reaction rate which can be computed using Eulerian-phase data for the CFD cell containing the particle. Because many Eulerian-phase source terms are proportional to the reaction rate, the accuracy of the particle-scale model can significantly affect the performance of reactor-scale CFD [5,9]. Therefore, to assess the accuracy of simple models for real biomass char morphologies, pore-resolving simulations can be used to calculate the "true" 3-D effectiveness factor using numerical integration,

$$\eta_{3-D} = \frac{\int\int\int R_{actual}(x_{O2}, T)dV}{\int\int\int R_{ideal}(x_{O2,s}, T)dV} \tag{2}$$

The actual reaction rate, R_{actual}, employs oxygen mole fraction, x_{O2}, data for each location in the microporous char, whereas the ideal rate, R_{ideal}, is calculated using a uniform mole fraction equal to the (surface averaged) value at the particle's surface, $x_{O2,s}$, which would prevail in the absence of internal diffusion limitations. Both actual and ideal rates use temperature, T, data for each local position in the char.

2.4. Spatially Resolved Effective-Continuum Model

Spatially resolved effective-continuum simulations (1-D, 2-D, or 3-D) are too expensive for particle-scale models in reactor-scale codes but are used as stand-alone models to study combustion fundamentals with arbitrarily complex submodels. The spatially resolved effective-continuum model treats all porosity at the subgrid-scale and employs the same effective-continuum conservation equations used for the microporous char regions of the pore-resolving simulations. All submodels and parameters for transport and reaction are identical to those used in the microporous char in the pore-resolving simulations, except for the subgrid-scale porosity, which is larger in the effective-continuum model, because the large pores are lumped into the subgrid-scale. The boundary conditions and solvers were identical to those used for the pore-resolving model. A finite cylindrical particle with uniform porosity and identical total volume to the pore-resolving particles (see Section 2.2) was meshed. The total porosity and aspect (length-to-radius) ratio, β, were chosen to be identical to one of the biomass char particles described in Section 3.

2.5. Effectiveness Factor Models

Analytical solutions for effectiveness factors have been developed for slabs, spheres, and cylinders, and approximations are available for more complex geometries. Due to the fibrous nature of many biomass feedstocks, cylindrical models may be best suited to the shape of many biochars, such as the pine char analyzed here, and are outlined concisely below, omitting long expressions available elsewhere.

The uniform finite cylinder (UFC) and uniform infinite cylinder (UIC) models treat particles as porous solid cylinders with uniform properties and exclusively subgrid-scale porosity. For the UFC, the geometry is 2-D and the analytical solution for the effectiveness factor, η_{UFC}, involves an infinite series and Bessel functions (see Eq. (12) in [26] based on [27]) and depends on the particle's Thiele modulus,

$$\phi_{UFC} = R\sqrt{\frac{k(1-\theta_{void})}{D_{eff}}} \tag{3}$$

and on the cylinder's aspect ratio, β.

The effective diffusivity, D_{eff}, and the intrinsic reaction rate constant, k, which incorporates the subgrid-scale surface area, were evaluated using identical submodels and parameters as used in the pore-resolving simulations for each real particle. The temperature (used in calculating k and D_{eff}) for a particle was obtained from a volume average over the microporous char region from that particle's pore-resolving simulation. (It will be seen in Section 3 that temperatures were nearly spatially uniform.) To ensure that the mass, volume, and subgrid-scale surface area of carbon in each 2-D UFC particle with subgrid-scale porosity matches that of its respective 3-D particle with resolved porosity, θ_{void}, the term (1- θ_{void}) is included in Eq. (3), as discussed in [18].

To ensure a faithful comparison with the pore-resolving simulations, the radius, R, used in the Thiele modulus for each particle was obtained from morphological measurements based on micro-CT for each specific particle. The particle's total volume is known (Section 2.2) and a bounding box method was used to measure its aspect ratio, β, defined as the ratio of the bounded length, to the bounded radius. The bounded length is taken directly from the length of the bounding box, and the bounded radius is approximated as half the average of the box's width and depth. Using the expression for the volume of a cylinder, the radius of the UFC particle is then:

$$R = \left({V_{Tot}}/{\pi\beta} \right)^{1/3} \tag{4}$$

The length of the particle is then given by

$$L = \beta R. \tag{5}$$

By using the bounding box method to obtain the dimensionless β, with its overestimation in both length and radial directions, and then calculating R by matching the volume of the cylinder to that of the real 3-D particle, a more accurate correspondence of geometric parameters is obtained than by taking R directly from bounding box measurements.

For the 1-D UIC model, which assumes a cylinder of infinite length, the classical expression for the effectiveness factor, η_{UIC}, involves Bessel functions of the first kind [28] and depends on the Thiele modulus, ϕ_{UIC}, which is given by the expression in Eq. (3). Again, to ensure a faithful comparison with the pore-resolving simulation for each biomass char particle, the radius, R, is obtained for each particle from Eq. (4) and all subgrid-scale parameters were identical to those used in the pore-resolving simulation.

Analytical solutions for hollow cylinders have also been derived since these geometries are often relevant to catalyst particles. In contrast to the UFC and UIC, which treat all porosity at the subgrid-scale, hollow cylinder models resolve a large, central cylindrical pore. Based on the work of Gunn [27], Buffham formulated analytical solutions for hollow finite cylinders and hollow infinite cylinders [29]. For a 2-D hollow finite cylinder, an "accessible" inner surface model will be considered (AHFC), such that the interface between the annulus and inner pore is exposed to the same concentration of reactant as the external surface (the same Dirichlet boundary conditions). For the 1-D hollow infinite cylinders, solutions for both accessible (AHIC) and inaccessible (IHIC) inner surfaces are available. For the IHIC, a no-flux boundary condition is applied at the inner surface and a fixed concentration is applied at the outer surface.

For the 2-D AHFC, η_{AHFC} is given by a complex expression involving several Bessel functions (Eq. (50) in [29]) and is omitted for brevity. The solution requires specification of inner and outer radii (R_{in} and R_{out}), the cylinder length (L), and depends on the nominal Thiele modulus,

$$\phi_{AHFC} = R_{out}\sqrt{\frac{k}{D_{eff}}} \tag{6}$$

To ensure a valid comparison between pore-resolving simulations and the hollow cylinder models, k, and D_{eff} were obtained using identical parameters and models, and the resolved porosity for each particle, θ_{void}, was taken directly from volume integration of segmented particle data from micro-CT. The outer radius, R_{out}, equals R, which was obtained from measurements of each particle, as shown in Eq. (4), L was obtained from Eq. (5), and R_{in} was calculated such that the core porosity equals the value of θ_{void} measured for each biomass char particle, by using

$$R_{in} = R_{out}\theta_{void}{}^{\frac{1}{2}} \tag{7}$$

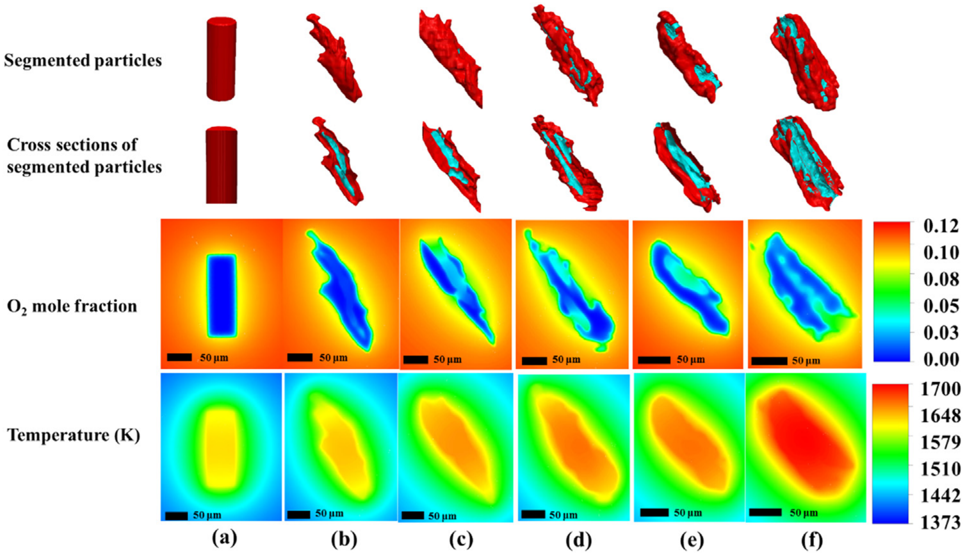

Fig. 2. Top row: 3-D geometries for a cylindrical effective continuum particle (column a) and five real, segmented biomass char particles (columns b, c, d, e, and f) showing microporous char in red and resolved pores in blue. Second row: cross-sections of the same particles. Third row: oxygen mole fraction distributions for the particle cross-sections, calculated from the simulations. Fourth row: temperature distributions for the particle cross-sections, calculated from the simulations.

Effectiveness factors for the 1-D AHIC and IHIC models are given in [29] (Eqs. (29) and (56) therein) and involve Bessel functions of the first and second kind, as well as the ratio of R_{in} to R_{out}. The nominal Thiele moduli are identical for the AHIC and IHIC models and are given by the expression in Eq (6).

To ensure a valid comparison between 3-D pore-resolving simulations and the 1-D AHIC and IHIC models, the resolved core porosity for each particle was set equal to its measured θ_{void}. Thus, R_{out} equals R, which was obtained from particle-specific measurements and Eq. (4) and R_{in} was again calculated using particle-specific θ_{void} and Eq. (7). Geometric parameters for all models are in Tables S1 and S4. Convergence of all series solutions was verified.

3. Results and Discussion

Zone II combustion of 30 biomass char particles with geometries obtained from high-resolution micro-CT was studied using the pore-resolving simulations. Fig. 2 shows the 3-D segmented geometries (top row) for five representative particles as well as an effective-continuum cylinder (column a) and cut-away views of the same segmented particles (second row). The particles are generally long and thin, with a mean aspect ratio of 6.25. This suggests that simple models based on cylindrical particles, rather than spherical particles, are more appropriate for this biomass char, as observed for many biomasses. It is also noted that even particles which appear externally non-porous can have significant internal porosity. For the 30 particles, the resolved (large pore) porosity, θ_{void}, ranged from 6.3% to 27.5%. In Lester's nomenclature [4], these chars would be classified as high-aspect ratio, porous (as opposed to cellular) structures.

Fig. 2 also shows distributions of oxygen mole fraction, x_{O2} (third row) and temperature (fourth row) for the same cross-sections, which pass through the center of the biomass char particles. It is noted that the x_{O2} distributions for the real biomass char particles are highly dependent on the morphology, as observed for coal chars undergoing zone II combustion [18]. Local minima in x_{O2} occur in the thick microporous char regions, irrespective of the distance from the particle surface. The large pores facilitate enhanced oxygen transport from the particle surface to its interior regions. This is somewhat similar to the impact of mm-scale cracks in larger biomass particles [20], but differs from the general observation that char oxidation is confined to the edges of mm-scale particles [21]. It is noted, however, that despite the significant porosity observed for "Particle B" (see Fig. 2, second row), x_{O2} is only slightly elevated in this particle's interior. This highlights the fact that large pores facilitate enhanced gas transport only if the pores penetrate the particle's external surface, which is only minimally the case for Particle B.

For the effective-continuum cylindrical particle (Particle A), all porosity is modeled at the subgrid-scale, and it is uniformly distributed. In this frequently used approach, large pores cannot facili-

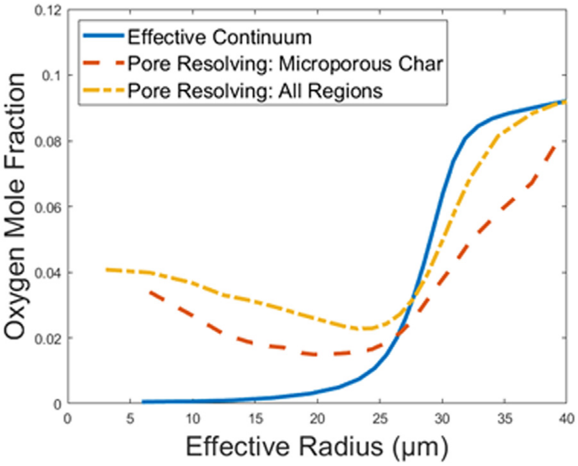

Fig. 3. Oxygen mole fraction as a function of effective radius, for the pore-resolving simulation and the spatially resolved effective continuum simulation.

tate oxygen diffusion into the particle interior, leading to a monotonic x_{O2} distribution, with the highest oxygen mole fraction at the external surface and the lowest oxygen mole fraction on the particle's central axis. It is noted that the total porosity of Particle A is identical to the total porosity (resolved + subgrid-scale) of Particle E, highlighting the importance of large pores in enhancing gas diffusion throughout the particle.

In contrast to x_{O2}, temperature distributions within all particles (effective-continuum and real biochar) are nearly spatially uniform throughout both the large pores and microporous char regions. Small temperature gradients are observed near the edges of the particles, but most of the gradients exist in the surrounding gas (the far-field boundary is at 1373 K). This is similar to the situation for pulverized coal char [18] and is due to the small particle sizes and high thermal conductivity resulting in small Biot numbers. Although temperature is relatively uniform within each particle, differences between particles are non-negligible. The effective-continuum particle has the lowest spatially averaged temperature (1609 K), whereas the particle with the highest oxygen penetration (Particle F) has the highest spatially averaged temperature (1680 K). Increasing levels of large porosity connected to the external surface led to higher oxygen penetration, higher char oxidation rates, more heat release, and higher temperatures.

To further examine the impacts of large pores and to compare oxygen penetration in real morphologies to effective-continuum predictions, Particles A and E, which have the same total porosity, were compared. Fig. 3 shows the directionally averaged oxygen mole fraction as a function of effective radius, which is calculated for the approximately cylindrical Particle E in the following manner. A set of 3-D iso-surfaces were created between the particle center and edge such that each point on an iso-surface is the same normal distance from the particle's edge. Then, the effective radius was defined using the relation between the surface area of a cylinder and its radius and length. First, the surface area of each irregular iso-surface layer, S_{layer}, is measured using surface integration. The aspect ratio of each layer, β_{layer}, is identical and is equal to β (Section 2.5). The effective radius, r_{eff}, for each iso-surface is then calculated by rearranging the expression for the area of a cylinder

$$r_{eff} = \sqrt{\frac{S_{layer}}{2\pi(1+\beta)}} \tag{8}$$

The oxygen mole fraction was then area-averaged over each iso-surface in two different ways. In the first method, the averaging was performed only over the microporous char regions, while in the second method, averaging was performed over both the microporous char and resolved pores (all regions).

When averaging over all regions, it is seen in Fig. 3 that the real biomass char particle has a higher x_{O2} in the particle interior than the effective continuum particle, as expected from the enhanced oxygen penetration in the large voids, seen in Fig. 2. However, even in the microporous char, x_{O2} is higher for the real particle than the effective continuum particle, despite the porosity of the microporous char being *lower* for the real particle (since the total porosity of the two particles is the same and the effective-continuum particle lumps all porosity at the subgrid-scale). The reason is likely that the elevated x_{O2} in real biomass char pores and the large interfacial area between those pores and the microporous char leads to enhanced penetra-

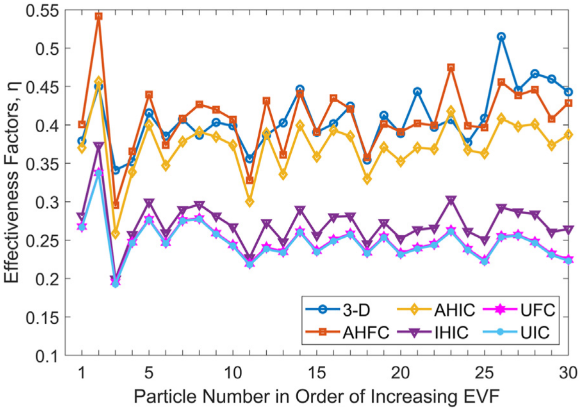

Fig. 4. Effectiveness factors for 30 particles calculated by 3-D pore resolving simulation and five analytical models.

tion into the microporous char. The characteristic length-scale for diffusion is thus decreased for the real biomass char particles. In contrast, for the effective continuum particle, oxygen must traverse the entire radius of the particle from its outer edge. Finally, it is noted that the higher x_{O2} at the outer edge for the effective continuum particle is likely caused by its higher porosity in the microporous char regions, as mentioned above. In the edge regions of both particles, oxygen diffuses primarily from the particle surface and the higher subgrid-scale porosity in Particle A leads to higher oxygen concentrations.

To assess the accuracy of particle-scale models amenable for use in reactor-scale CFD, "true" effectiveness factors from 3-D pore-resolving simulations (Eq. (2)) for all 30 particles are compared to those predicted by the analytical models (Section 2.5) in Fig. 4. It is recalled that for each particle, the analytical solutions employed the particle's specific morphological parameters obtained from micro-CT imaging. Particles are arranged on the abscissa by particle number (one to 30) in order of increasing external void fraction, EVF, which is the fraction of the particle's external surface that is penetrated by large pores (or "voids"). EVF was well-correlated with $\eta_{3\text{-}D}$ for coal char particles [18], but neither EVF nor any single measured morphological parameter (e.g., porosity, aspect ratio, surface area, etc.) correlated particularly well with $\eta_{3\text{-}D}$ for these biomass chars. It is noted that although each particle had identical size (total volume, see Section 2.2), $\eta_{3\text{-}D}$ ranged between 34.1% and 51.5%.

As seen in Fig. 4, the two purely subgrid-scale porosity models, UFC and UIC, predict similar effectiveness factors, which is due to the high aspect ratio of the pine char particles. Both models significantly underpredict the effectiveness factors, due to their neglect of the impact of large, connected pores serving as reactant conduits. The uniform models thus overestimate the characteristic diffusion length and the level of diffusion limitations. The relative errors averaged for all particles for the UFC and UIC are 38.6% and 39.0%, respectively. For these types of biomass particles, employing typical (subgrid-scale) uniform porosity effectiveness factor models for cylinders in reactor-scale CFD codes would lead to significant underprediction of the reaction rate.

Based on Fig. 2, hollow cylinders appear to approximate the morphology of the pine char particles with greater accuracy than uniform cylinders. While the IHIC model severely underpredicts $\eta_{3\text{-}D}$ (average relative error 33.1%) since the inaccessible inner surface forces oxygen to be transported across the entire annular thickness, the AHIC and AHFC models, with accessible inner surfaces, reproduce the effectiveness factors for the pine char particles with better accuracy. As expected, the 2-D AHFC predicts slightly higher effectiveness factors than the infinite (1-D) AHIC. Both of these models capture the reduced length-scale for oxygen diffusion, which is now approximately equal to half the annular thickness. Although "fully accessible" models overestimate the level of x_{O2} on the interface between large pores and microporous char, based on Fig. 2 (which leads to overestimations of η), they also underestimate the interfacial area and overestimate the local thickness of microporous char regions. These two factors would lead to underestimations of η, counteracting the impact of the fully accessible assumption. The average relative errors for the AHIC and AHFC are 9.0% and 6.0%, respectively. In contrast to mm-scale particles with many parallel pores that experience diffusion primarily in the axial direction (i.e., slab behavior) [2], these smaller, μm-scale char particles contain fewer, more irregular large pores, experience significant radial diffusion (Fig. 2), and are more accurately modeled as hollow cylinders

(Fig. 4). For particle-scale modeling in reactor-scale CFD codes, the use of a 1-D accessible hollow cylinder model (AHIC) could provide an accurate and computationally-efficient solution for pulverized pine char particles and other similar biomass chars.

4. Conclusions

Geometrically faithful, pore-resolving, zone II combustion simulations have been performed for real pulverized biomass char particle morphologies for the first time. Pine char particles imaged with high-resolution micro-CT had anisotropic, porous structures and exhibited non-monotonic oxygen mole fraction distributions facilitated by enhanced diffusion in large pores that were connected to the external surface. Effective-continuum simulations underpredicted reactant penetration into the particle, even in the microporous char regions that surround the large pores. Similarly, uniform effectiveness factor models, which are often used as particle-scale models in reactor-scale codes, significantly underpredicted the effectiveness factors compared to results from the geometrically faithful simulations. Hollow cylinder effectiveness factor models with fully accessible inner surfaces exhibited better agreement with results for the real particles, although these models incorporate assumptions with counterbalancing inaccuracies.

Declaration of Competing Interest

The authors declare that they have no known competing financial interests or personal relationships that could have appeared to influence the work reported in this paper.

Acknowledgements

This work was partially supported by the NSF (Award Number CBET-2211062). Support from the Michael J Wallace Endowed Faculty Scholars Fund in Energy Leadership is gratefully acknowledged. This research used the Raj high-performance computing facility funded by the National Science foundation award CNS-1828649 and Marquette University. The authors thank April Neander and Prof. Zhe-Xi Luo at the University of Chicago Paleo-CT lab for imaging and Colton Herbert for assistance with char preparation.

Supplementary materials

Supplementary material associated with this article can be found, in the online version, at doi:10.1016/j.proci.2022.07.098.

References

[1] H. Fatehi, W. Weng, Z. Li, X.-S. Bai, M. Aldén, Recent Development in Numerical Simulations and Experimental Studies of Biomass Thermochemical Conversion, Energy & Fuels 35 (2021) 6940–6963, doi:10.1021/acs.energyfuels.0c04139.

[2] H. Watanabe, X-ray Computed Tomography Visualization of the Woody Char Intraparticle Pore Structure and Its Role on Anisotropic Evolution during Char Gasification, Energy and Fuels 32 (2018) 4248–4254, doi:10.1021/acs.energyfuels.7b03227.

[3] U. Kleinhans, S. Halama, H. Spliethoff, Char particle burning behavior: Experimental investigation of char structure evolution during pulverized fuel conversion, Fuel Process. Technol. 171 (2018) 361–373, doi:10.1016/j.fuproc.2017.10.022.

[4] E. Lester, C. Avila, C.H. Pang, O. Williams, J. Perkins, S. Gaddipatti, G. Tucker, J.M. Barraza, M.P. Trujillo-Uribe, T. Wu, A proposed biomass char classification system, Fuel 232 (2018) 845–854, doi:10.1016/j.fuel.2018.05.153.

[5] P.N. Ciesielski, M.B. Pecha, N.E. Thornburg, M.F. Crowley, X. Gao, O. Oyedeji, H. Sitaraman, N. Brunhart-Lupo, Bridging Scales in Bioenergy and Catalysis: A Review of Mesoscale Modeling Applications, Methods, and Future Directions, Energy and Fuels 35 (2021) 14382–14440, doi:10.1021/acs.energyfuels.1c02163.

[6] S.R. Gubba, L. Ma, M. Pourkashanian, A. Williams, Influence of particle shape and internal thermal gradients of biomass particles on pulverised coal/biomass co-fired flames, Fuel Process. Technol. 92 (2011) 2185–2195, doi:10.1016/j.fuproc.2011.07.003.

[7] S. Schulze, A. Richter, M. Vascellari, A. Gupta, B. Meyer, P.A. Nikrityuk, Novel intrinsic-based submodel for char particle gasification in entrained-flow gasifiers: Model development, validation and illustration, Appl. Energy. 164 (2016) 805–814, doi:10.1016/j.apenergy.2015.12.018.

[8] X. Ku, J. Wang, H. Jin, J. Lin, Effects of operating conditions and reactor structure on biomass entrained-flow gasification, Renew. Energy 139 (2019) 781–795, doi:10.1016/j.renene.2019.02.113.

[9] P.N. Ciesielski, M.B. Pecha, A.M. Lattanzi, V.S. Bharadwaj, M.F. Crowley, L. Bu, J.V. Vermaas, K.X. Steirer, M.F. Crowley, Advances in Multiscale Modeling of Lignocellulosic Biomass, ACS Sustain. Chem. Eng 8 (2020) 3512–3531, doi:10.1021/acssuschemeng.9b07415.

[10] A.G. Borrego, L. Garavaglia, W.D. Kalkreuth, Characteristics of high heating rate biomass chars prepared under N2 and CO2 atmospheres, Int. J. Coal Geol. 77 (2009) 409–415, doi:10.1016/j.coal.2008.06.004.

[11] C.H. Pang, E. Lester, T. Wu, Influence of lignocellulose and plant cell walls on biomass char morphology and combustion reactivity, Biomass and Bioenergy 119 (2018) 480–491, doi:10.1016/j.biombioe.2018.10.011.

[12] A. Panahi, N. Vorobiev, M. Schiemann, M. Tarakcioglu, M. Delichatsios, Y.A. Levendis, Combustion details of raw and torrefied biomass fuel particles with individually-observed size, shape and mass, Combust. Flame. 207 (2019) 327–341, doi:10.1016/j.combustflame.2019.06.009.

[13] P.N. Ciesielski, M.F. Crowley, M.R. Nimlos, A.W. Sanders, G.M. Wiggins, D. Robichaud, B.S. Donohoe, T.D. Foust, Biomass Particle Models with Realistic Morphology and Resolved Microstructure for Simulations of Intraparticle Transport Phenomena, Energy & Fuels 29 (2015) 242–254, doi:10.1021/ef502204v.

[14] C. Di Blasi, Combustion and gasification rates of lignocellulosic chars, Prog. Energy Combust. Sci. 35 (2009) 121–140, doi:10.1016/j.pecs.2008.08.001.

[15] S. Whitaker, The Method of Volume Averaging, 1st Editio, Springer, Netherlands, Boston, 1999.

[16] E.M. Hodge, D.G. Roberts, D.J. Harris, J.F. Stubington, The Significance of Char Morphology to the Analysis of High-Temperature Char−CO2 Reaction Rates, Energy & Fuels 24 (2010) 100–107, doi:10.1021/ef900503x.

[17] G. Fong, S. Jorgensen, S.L. Singer, Pore-Resolving Simulation of Char Particle Gasification Using Micro-CT, Fuel 224 (2018) 752–763, doi:10.1016/j.fuel.2018.03.117.

[18] D. Liang, S. Singer, Pore-Resolving Simulations to Study the Impacts of Char Morphology on Zone II Combustion and Effectiveness Factor Models, Combust. Flame. 229 (2021) 111405.

[19] F. Mermoud, F. Golfier, S. Salvador, L. Van De Steene, J.L. Dirion, Experimental and Numerical Study of Steam Gasification of a Single Charcoal Particle, Combust. Flame. 145 (2006) 59–79, doi:10.1016/j.combustflame.2005.12.004.

[20] E. Boigné, N.R. Bennett, A. Wang, K. Mohri, M. Ihme, Simultaneous in-situ measurements of gas temperature and pyrolysis of biomass smoldering via X-ray computed tomography, Proc. Combust. Inst. 38 (2021) 3899–3907, doi:10.1016/j.proci.2020.06.070.

[21] E. Boigné, N.R. Bennett, A. Wang, M. Ihme, Structural analysis of biomass pyrolysis and oxidation using in-situ X-ray computed tomography, Combust. Flame 235 (2022) 111737, doi:10.1016/j.combustflame.2021.111737.

[22] S. Hjärtstam, K. Andersson, F. Johnsson, B. Leckner, Combustion characteristics of lignite-fired oxy-fuel flames, Fuel 88 (2009) 2216–2224, doi:10.1016/j.fuel.2009.05.011.

[23] S.V. Sotirchos, N.R. Amundson, Dynamic Behavior of a Porous Char Particle Burning in an Oxygen–Containing Environment. Part I. Constant Particle Radius, AIChE J 30 (1984) 537–549.

[24] K.B. Bischoff, Accuracy of the Pseudo Steady State Approximation for Moving Boundary Diffusion Problems, Chem. Eng. Sci. 18 (1963) 711–713.

[25] D. Luss, On the Pseudo Steady State Approximation for Gas Solid Reactions, Can. J. Chem. Eng. 46 (1968) 154–156.

[26] M. Asif, Efficient expressions for effectiveness factor for a finite cylinder, Chem. Eng. Res. Des. 82 (2004) 605–610, doi:10.1205/026387604323142658.

[27] D.J. Gunn, Diffusion and chemical reaction in catalysis and absorption, Chem. Eng. Sci. 22 (1967) 1439–1455.

[28] C.N. Satterfield, Mass Transfer in Heterogeneous Catalysis, 1st ed., M.I.T. Press, 1970.

[29] B.A. Buffham, Design relations for hollow catalyst pellets, Trans. Inst. Chem. Eng. A. 78 (2000) 269–282, doi:10.1205/026387600527130.